Optimized design and mechanical properties of TPMS porous structures based on selective laser sintering

Heng-Liang Fan[1,2] (iD), Abdullah Yassin[1], Khairul Fikri Tamrin[1], Sinin Hamdan[1], Chao Wang[2]

[1]Universiti Malaysia Sarawak, Faculty of Engineering. 94300, Kota Samarahan, Sarawak, Malaysia.

[2]Bengbu University, School of Mechanical and Vehicle Engineering, Bengbu. 233030, Bengbu, Anhui, China.

e-mail: yabdulla@unimas.my, fhl209@126.com, 22010200@siswa.unimas.my, hsinin@unimas.my, wjick1990@126.com

ABSTRACT

Triply periodic minimal surface (TPMS) structures are commonly used for lightweight and energy-absorption applications. TPMS structures have a high porosity and are prone to the pinch-off phenomenon. In this study, we designed primitive and Schoen I-graph-wrapped package (I-WP) structures with different porosities. An optimized design function was introduced to obtain a high-porosity P-I structure, which was less prone to pinch off. The mechanical properties of the structures with different porosities achieved using selective laser sintering technology were investigated. Results showed that the porosities of primitive, I-WP, and P-I structures exhibited different correlations with the constant t. The elastic modulus and yield strength of all three structures decreased with porosity. For the same porosity, the compressive strength and elastic modulus of the P-I porous structure exceeded those of the primitive and I-WP porous structures. Additionally, the primitive porous structure was predominantly in the stretching deformation mode, whereas the I-WP and P-I structures were mostly in the stretching and bending deformation modes. The P-I porous structure showed better energy-absorption properties than the primitive and I-WP structures. This study enriched extremely small-surface porous structures and provided a relevant basis for their application in engineering fields.

Keywords: Selective laser sintering; Triply periodic minimal surfaces; Porosity; Mechanical properties.

1. INTRODUCTION

Triply periodic minimal surface (TPMS) porous structures are smooth and have fully connected internal structures, large specific surface areas, and good mechanical properties [1, 2]. Additive manufacturing techniques such as selective laser melting (SLM),fused deposition modeling (FDM) and selective laser sintering (SLS) are used to form complex parts [3–6]. These techniques provide technical support for the preparation of TPMS porous structures and can effectively solve many problems, such as difficulty in accurately controlling the porosity and pore size of structures in traditional porous structure preparation methods [7]. Thus, TPMS porous structures prepared by additive manufacturing techniques are widely used in several fields, such as aerospace [8], biomedicine [9], and mechanical manufacturing fields [10].

However, when the porosity is higher than a certain value, the problem is that the classic TPMS functions cannot be obtained with a continuous structure. This problem also is named as pinch-off. A significant weakness in the traditional TPMS functions is the pinch-off problem, which can result in structural design issues and stress concentration. The constraints in designing the spectrum of porosity are the structural issue. Several studies have been conducted to create an optimal design for TPMS porous structures and the preparation of TPMS porous structures by additive manufacturing techniques. Rajagopalan *et al*. established a Gyroid implicit function to derive a mathematical description of the TPMS porous structure [11]. Porous structures can be created with different porosities by modifying a specific implicit function constant. According to the Gyroid implicit function, YANG *et al*. used MATLAB to generate a program for porous structures and additive manufacturing techniques to fabricate the structures [12]. LIU *et al*. [13] proposed Gyroid and Diamond unit cells based on the TPMS implicit function. Relative density and constant t in implicit function are shown to be related to the Gyroid and Diamond unit cells. Results show that pinch-off occurs when constant t exceeds 1.2. However, the pinch-off phenomenon has not been studied in depth. LI *et al*. [14] proposed to add a penalty function to the classical Gyroid implicit surface function to solve the pinch-off phenomenon of porous structures. Thus, based on the new function, a Gyroid structure with high porosity can be obtained. However, the performance of the optimized

structure was not compared in their work. It fails to verify the feasibility of the optimized structure. Studies on the design of TPMS porous structures and performance have focused primarily on Gyroid and Diamond porous structures [15, 16].

Although the pinch-off problem in TPMS porous structures has been studied in some detail, little research has been done on the ideal control parameter to use when modelling TPMS porous structures. Therefore, the present work proposed an optimization method based on pore characteristic parameters to produce structures with high porosity. We aimed to address the pinch-off issue presented during the design process of P and I-WP porous structures. The structure was fabricated using SLS technique. The compressive properties and energy-absorption characteristics of the structures with different porosities were also investigated. This study provided a theoretical basis for the preparation of extremely small curved porous structures by using additive manufacturing techniques for engineering applications.

2. MATERIALS AND METHODS

2.1. Design of TPMS porous structures

A TPMS is a minimal surface on a three-dimensional cycle determined by a specific mathematical function. The surface is characterized by periodic variations in three directions in space. The modeling methods for preparing TPMS structures can generally be classified as boundary, implicit function, and parametric methods. An accurate modeling method uses the Weierstrass function, but ensuring the accuracy of the surface with this parametric form is difficult. Implicit periodic surfaces are typically used for the approximate representation of TPMS surfaces, as shown in Equation (1)[17]:

$$\varphi(r) = \sum_1^k A_k \ \cos[2\pi(h_k r) \ / \ \delta_h + p_k] \ - \ t = 0 \tag{1}$$

Where r is the position vector in Euclidean space, h_k is the kth lattice vector in inverse space, A_k is the amplitude factor, k is the wavelength of the cycle, p_k is the phase, and t is a constant.

Four common TPMS structures are Gyroid, Diamond, Primitive, and I-WP [18]. Primitive and I-WP porous structures have good manufacturing performance; hence, they were selected in this study. The mathematical expressions for the implicit surface structure are given as Equations (2) and (3):

$$F_P = \cos\left(\frac{2\pi}{L} \cdot x\right) + \cos\left(\frac{2\pi}{L} \cdot y\right) + \cos\left(\frac{2\pi}{L} \cdot z\right) \ - \ t \tag{2}$$

$$F_{I-WP} = \cos\left(\frac{2\pi}{L} \cdot x\right)\cos\left(\frac{2\pi}{L} \cdot y\right) + \cos\left(\frac{2\pi}{L} \cdot y\right)\cos\left(\frac{2\pi}{L} \cdot z\right) + \cos\left(\frac{2\pi}{L} \cdot z\right)\cos\left(\frac{2\pi}{L} \cdot x\right) - \ t \tag{3}$$

Where L is the edge length of the TPMS cell (in mm), and t is a constant that can be controlled to obtain minimal surfaces with different porosities. However, a value of t exceeding a certain range produces a porosity greater than a specific value, causing discontinuities in the minimal surfaces. Then, a pinch-off phenomenon can then occur, inhibiting the formation of porous structures during fabrication [19]. According to Equations (2) and (3), the minimal value surfaces and closed unitary bodies of primitive and I-WP can be obtained using MATLAB and Materialise Magics software, as shown in Figure 1.
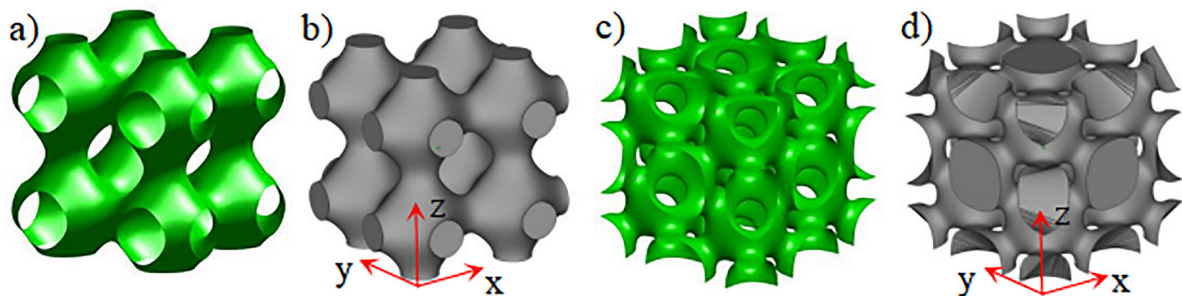

Figure 1: TPMS porous structure: (a) primitive minimum surface; (b) primitive closed unit body; (c) I-WP minimal surface; (d) I-WP closed unitary body.

MATLAB was used to visualize the relationship between porosity ρ^* and t for different values of t, as shown in Figure 2(a) and (b). The porosity ρ for the primitive porous structure is linearly related to t; the porosity ρ^* increases as t increases ($-0.9 \leq t \leq 0.9$). When the value of t is exceeded, a pinch-off phenomenon occurs, i.e., primitive porous structures with porosity above 73.05% are not printed. The porosity P of I-WP porous structures is a quadratic function of t. The porosity ρ^* increases as t increases ($-0.9 \leq t \leq 0$). When the value of t is exceeded, a pinch-off phenomenon also occurs, i.e., I-WP porous structures with a porosity of 61.48% and above are not printed or formed.

By optimizing the implicit function of the initial minimal surface, a new function is introduced, as shown in Equation (4), to form structures with a high porosity while avoiding the pinch-off phenomenon.

$$F_{opt} = a * F_P' + b * F_{I-WP}' - t \tag{4}$$

The added function is an optimization function based on the primitive and I-WP implicit surface functions. New porous structures can be obtained by adjusting the coefficients a, b, and t to form the P-I porous structure. In the new function, parameter a is first set to 10, and the pinch-off behavior of the structure is controlled by adjusting parameter b. When $b \leq 3$, the pinch-off phenomenon of the primitive structure still occurs, but as the value of b increases, the pinch-off problem is slowly resolved. However, when $b \geq 7$, the primitive unitary structure reverts to the pinch-off state. Therefore, b is set to 5 to obtain optimized stable structures. The expression of the optimized implicit function is given as shown in Equation (5):

$$\begin{aligned} F_{opt} = 10\Bigg[&\cos\left(\frac{2\pi}{L} \cdot x\right)\cos\left(\frac{2\pi}{L} \cdot y\right) + \cos\left(\frac{2\pi}{L} \cdot y\right)\cos\left(\frac{2\pi}{L} \cdot z\right) + \cos\left(\frac{2\pi}{L} \cdot z\right)\cos\left(\frac{2\pi}{L} \cdot x\right)\Bigg] \\ &- 5\Bigg[\cos\left(\frac{4\pi}{L} \cdot x\right) + \cos\left(\frac{4\pi}{L} \cdot y\right) + \cos\left(\frac{4\pi}{L} \cdot z\right)\Bigg] - t \end{aligned} \tag{5}$$

P-I porous structures with a high porosity are obtained by adjusting the value of t. The relationship among porosity ρ^*, constant t, and the fitted function curve is illustrated in Figure 3. This finding indicates that the optimized P-I porous structure can obtain a porosity of up to 92.78% without pinch-off occurring. The figure shows a quadratic function between porosity ρ^* and threshold t, which is more similar to the I-WP porous structure.

2.2. Materials

Nylon (PA2200) powder was used with SLS technology. The process parameters were as follows: 22 W filling laser power, 1200 mm·s^{-1} scanning speed, and 0.12 mm powder thickness. Primitive and I-WP porous structures with 40%, 50%, and 60% porosities were formed. The P-I optimized porous structures with 65%, 75%, and 85% porosity were also formed; the design models and printed specimens are shown in Figure 4(c). The dimensions were 32 mm × 32 mm × 32 mm, and three specimens were formed for each group.
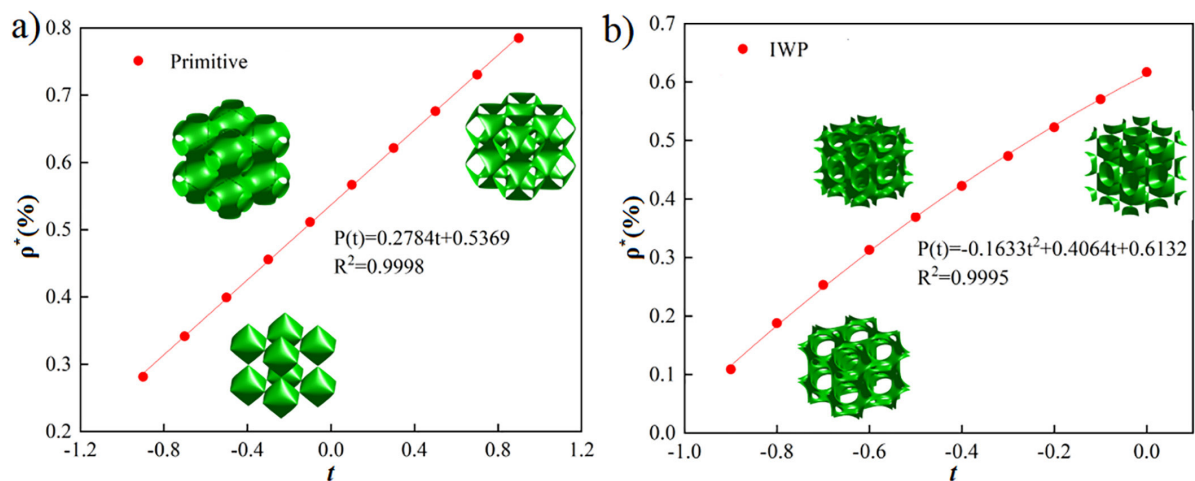

Figure 2: Relationship between porosity ρ^* and threshold t of TPMS structure: (a) primitive; (b) I-WP.
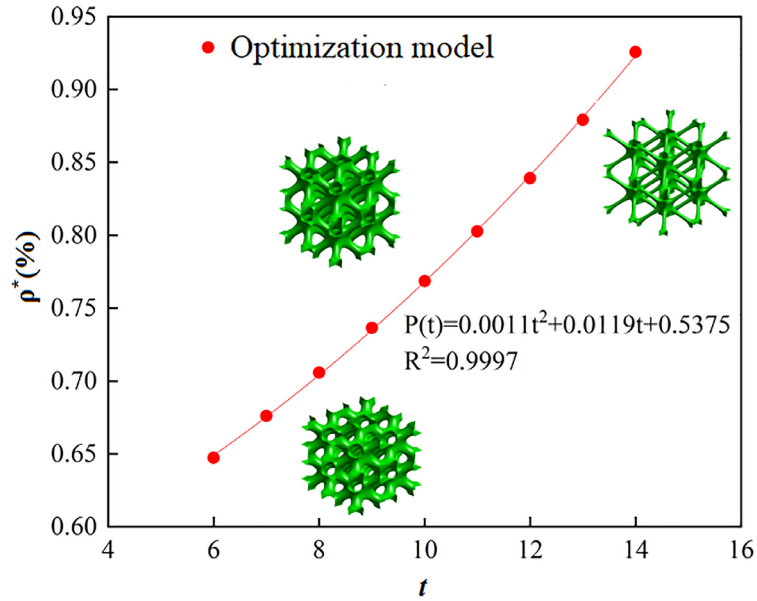
Figure 3: Relationship between porosity ρ* and threshold t of the P-I porous structure.
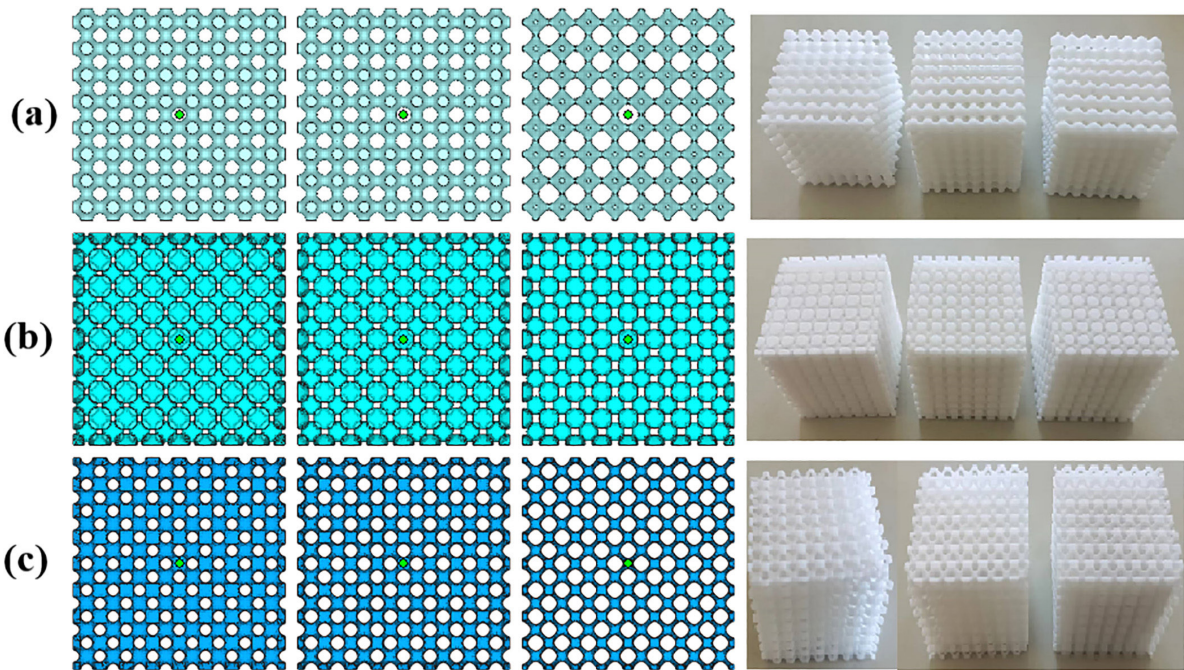

Figure 4: Design models and printed samples: (a) primitive; (b) I-WP; (c) P-I.

2.3. Experiment

According to ASTM standard D1621, uniaxial compression tests were conducted on the formed parts by using a DNS300 electronic universal testing machine (Jinan Xinshijin Test Instrument Co., China, DNS300) at a constant loading speed of 2 mm/min. The maximum loading force of the machine was 100 kN. The samples were tested perpendicular to the print direction, with the specimens placed in the center of the loading plate to ensure loading uniformity and prevent misalignment. The entire compression process was recorded in the video recorded. The elastic modulus of the structure was calculated from the slope of the initial linear region of the compression stress–strain curve, and the plateau stress was defined as the mean stress over the strain range of 0.2 to 0.5.

3. RESULTS AND DISCUSSION

3.1. Compression performance analysis

After data acquisition, origin was used to plot the compression stress-strain curves for the primitive, I-WP, and P-I porous structures, and results are shown in Figure 5. The elastic modulus and yield strength are presented in Table 1.
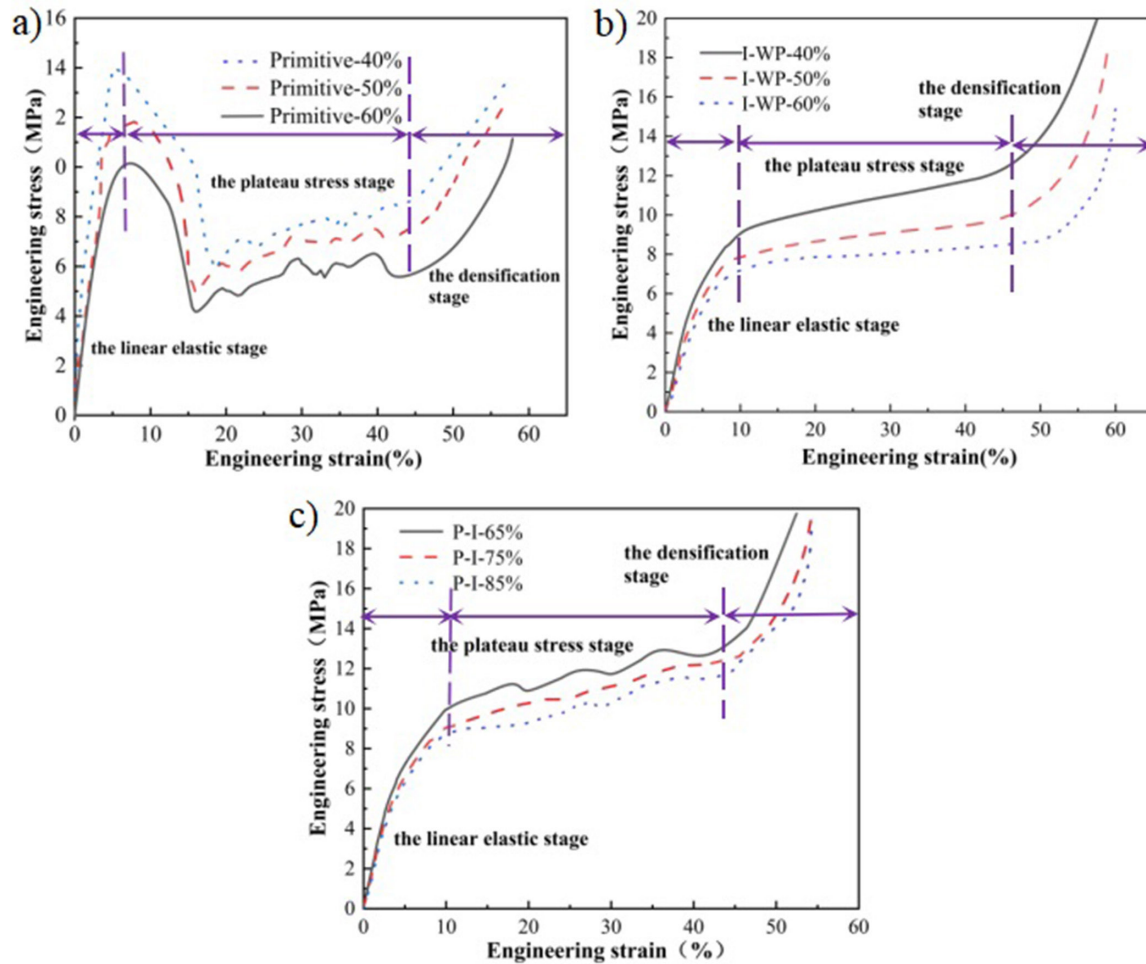

Figure 5: Stress–strain curves of porous structures: (a) primitive; (b) I-WP; (c) P-I.

Table 1: Elastic modulus and yield strength of TPMS porous samples.

TYPE	POROSITY(%)	ELASTIC MODULUS (MPa)	YIELD STRENGTH (MPa)
Primitive	40	96.33 ± 2.76	13.56 ± 0.56
	50	74.14 ± 2.37	10.82 ± 0.75
	60	59.28 ± 2.64	9.18 ± 0.44
I-WP	40	81.51 ± 2.86	8.38 ± 0.37
	50	66.69 ± 2.32	7.14 ± 0.45
	60	44.46 ± 2.64	6.13 ± 0.28
P-I	65	64.47 ± 2.47	9.26 ± 0.52
	75	62.24 ± 2.38	8.53 ± 0.34
	85	55.58 ± 2.52	7.81 ± 0.48

Figure 5 and Table 1 show that an increase in porosity leads to a decrease in compressive strength and elastic modulus across all varieties of TPMS porous structures. From Table 1, yield strength of primitive porous structures are from 9.18 ± 0.44 to13.56 ± 0.56 MPa as porosity decreases from 60% to 40%. The elastic modulus decreases from 96.33 ± 2.76 MPa to 59.28 ± 2.64 MPa. Thus, as the porosity increases, the yield strength and elastic modulus of primitive structures decrease gradually. Similarly, as shown in Table 1, as the porosity increases from 40% to 60%, the yield strength and elastic modulus of I-WP structures also decrease gradually. The results show that when porosity was held at 60%, the primitive structures (P) exhibited an elastic modulus of 59.28 ± 2.64 MPa and a yield strength of 9.18 ± 0.44 MPa. In contrast, the I-WP structures showed an elastic modulus of 44.46 ± 2.64 MPa and a yield strength of 6.13 ± 0.28 MPa. These findings suggest that primitive structures provide better mechanical performance than I-WP structures at the same level of porosity. The yield strength and elastic modulus of the P-I porous structure with 65% porosity were 9.26 ± 0.52 MPa and 64.47 ± 2.47 MPa, respectively, which were higher than those of the primitive porous structure with 60% porosity. The yield strength and elastic modulus of the P-I porous structure with 85% porosity were 7.81 ± 0.48 MPa and 55.58 ± 2.52 MPa, respectively, which were higher than those of the I-WP porous structure with 50% porosity. With porosity levels set at 60% for Primitive and I-WP, and 65% for P-I, the elastic modulus and yield strength of P-I are the highest, recorded at 64.47 ± 2.47 MPa and 9.26 ± 0.52 MPa, respectively. Consequently, this demonstrates that the porous structure of P-I possesses outstanding mechanical properties compared with P-I and I-WP.

In Figure 5(a), the stress-strain curve of the primitive structure in the linear elastic stage showed a linear relationship; strain hardening occurred, and after the structure yields, it entered the elastic-plastic deformation stage. This behavior aligns with the findings presented in reference [20]. At the peak of the plastic-yielding plateau stage, the curve showed irregular fluctuations, indicating extreme instability of the structure. As deformation continued, stress increased sharply, and the porous structure entered the densification stage, manifesting as a structural failure. Local softening or fracture at the unit joints of the P structure began when it passed through the linear elasticity stage and yielding. The stress-strain curve exhibited erratic fluctuation between ups and downs as it moved into the third stage of fluctuating yielding. The unit junctions of the porous structure came into contact with one another as the strain increased, and the structure began to densify.

The I-WP and optimized P-I structures had similar compression curves. The entire compression process can be categorized into a linear elastic deformation stage, plastic yield plateau stage, and compaction stage, among which the plastic yield plateau stage was the longest. When the strength of the porous structure reached its yield limit, the plastic yield plateau stage occurred slowly. During this phase, the optimized P-I porous structure differed from the I-WP structure as fluctuations in its stress occurred. This phenomenon occurred because the structure is optimized as a combination of both primitive and I-WP types, where it showed some characteristics similar to those of the primitive type in the plastic yield plateau.

The compression behaviour of the primitive and I-WP porous structures with 50% porosity and that of the P-I porous structure with 75% porosity are shown schematically in Figure 6. The primitive porous structure was deformed along the central surface during compression but showed good mechanical properties. The I-WP and P-I barrelled after external loading and showed crushing signs at the stress concentration.

To establish a better design guide for individual porous structures, the Gibson-Ashby equation was used to describe the relationship among elastic modulus, compressive strength, and relative density. Accordingly, the relationship between the design parameters of porous structures and their mechanical properties was obtained. Based on experimental results, a mathematical model of the mechanical properties and porosity of the porous structures was first fitted by the Gibson-Ashby theoretical model. This step was concatenated with the equation of the relationship between the design parameters and porosity derived from the design section of the porous structures. Mathematical expressions for the Gibson–Ashby predictive model for the TPMS structures are given as Equations (6) and (7) [21].

$$E^* = \frac{E}{E_s} = c_1 \left(\frac{\rho}{\rho_s} \right)^{n_1} \tag{6}$$

$$\sigma^* = \frac{\sigma}{\sigma_s} = c_2 \left(\frac{\rho}{\rho_s} \right)^{n_2} \tag{7}$$

Where E, σ, and ρ are the elastic modulus, yield strength, and porous structure density, respectively. E_s, σ_s, and ρ_s are the elastic modulus, yield strength, and density of the corresponding dense material, respectively. E/E_s,

σ/σ_s, and ρ/ρ_s are the relative elastic modulus, relative yield strength, and relative density, respectively. c_1 and c_2 are design parameters. n_1 and n_2 are scaling constants whose values are related to the lattice pattern of the porous structure. The value of n can determine the different modes of deformation (stretching, bending, or mixed mode of deformation) of the porous structure. The fitted curves showing relative yield strength σ^*, relative elastic modulus E^*, and relative density ρ^* can be obtained by fitting power functions, as illustrated in Figure 7.

Figure 7 shows that with porosity increased, the relative elastic modulus and relative yield strength of the three porous structures increased. For the same porosity, the $E^* - \rho^*$ and $\sigma^* - \rho^*$ curves of the primitive structure were higher than those of the I-WP structure, indicating that the former had excellent mechanical properties.

According to the Gibson-Ashby model and the fitted results, the proportionality constants n_1 and n_2 of the primitive porous structure were close to 1. This finding indicated that the structure was in a predominantly tensile-deformation mode. Conversely, the proportionality constants n_1 and n_2 of the I-WP and P-I porous structures are between 0 and 2, indicating that these structures were predominantly deformed in tensile and bending modes. This is in agreement with the results reported on metallic cellular lattices by MA *et al.* [22]. The fitted values and error percentages for the relative elastic modulus and relative yield strength are presented in Table 2. The maximum error percentage of the relative elastic modulus and relative yield strength are 3.1% and 2.7%, respectively. Both were less than 5%, indicating that the fitted results are within the error tolerance.
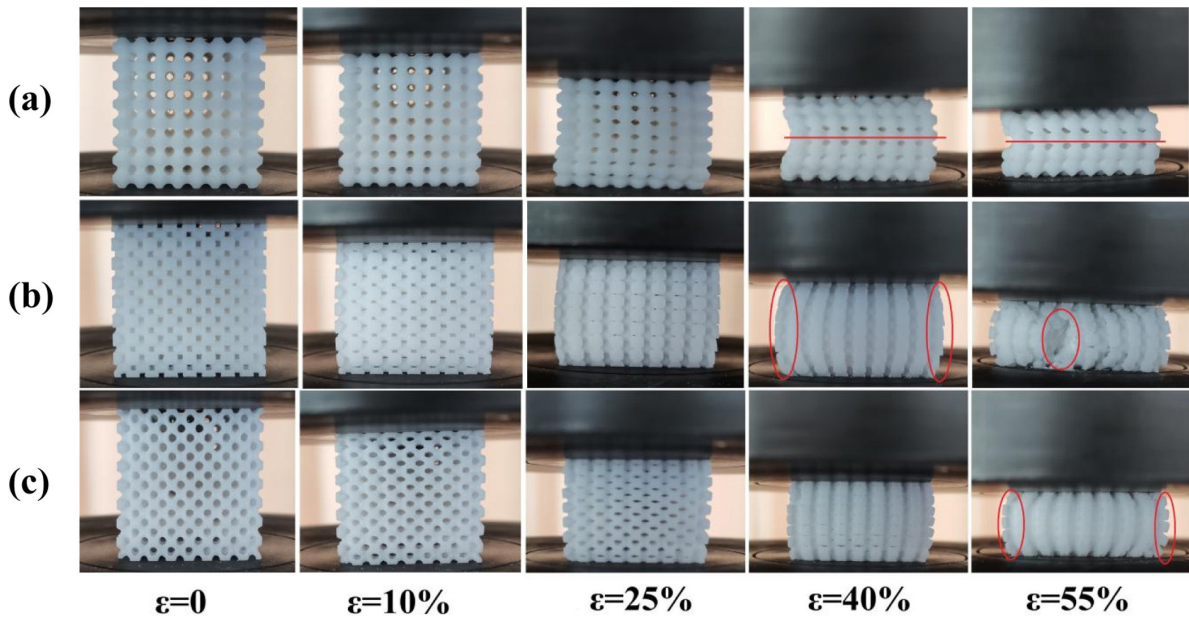

Figure 6: Compression behavior of different porous structures: (a) primitive; (b) I-WP; (c) P-I.
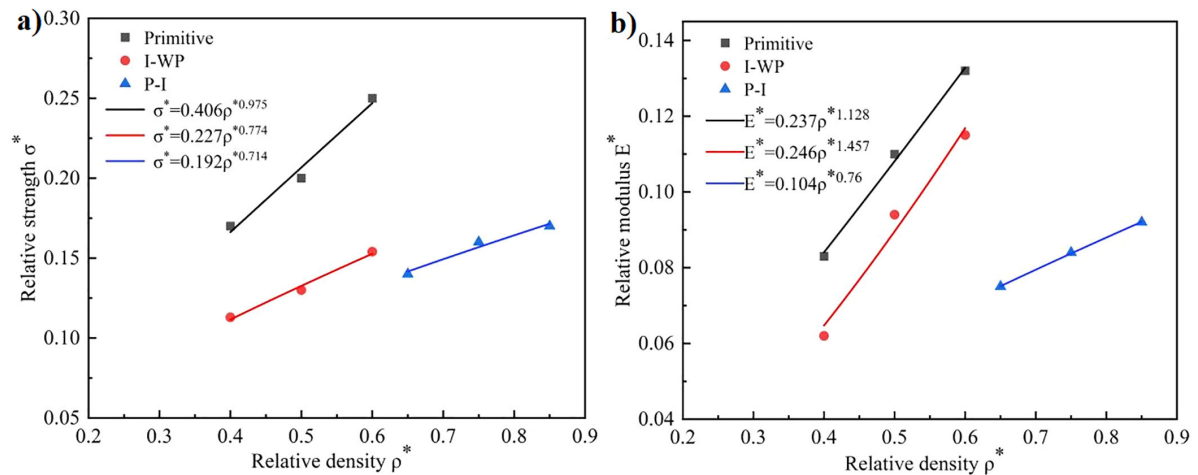

Figure 7: (a) Relative strength–density fitted lines; (b) relative modulus–density fitted lines.

Table 2: Fitting values and error percentages of relative elastic modulus and yield strength.

TYPE (%)	RELATIVE ELASTIC MODULUS, E*		RELATIVE YIELD STRENGTH, σ*	
	FITTING VALUES	ERROR PERCENTAGE (%)	FITTING VALUES	ERROR PERCENTAGE (%)
Primitive: 40	0.084	1.2	0.166	2.3
Primitive: 50	0.108	1.8	0.266	2.7
Primitive: 60	0.133	0.7	0.247	1.2
I-WP: 40	0.063	1.6	0.112	0.8
I-WP: 50	0.089	3.1	0.133	2.3
I-WP: 60	0.116	0.8	0.153	0.6
P-I: 65	0.075	0.1	0.141	0.7
P-I: 75	0.0836	0.5	0.156	2.5
P-I: 85	0.092	0.1	0.171	0.6

3.2. Energy-absorption characteristics

Energy-absorption characteristics are important evaluation indicators for porous structures [23]. The formula for calculating energy absorption in porous structures is expressed in Equation (8).

$$W_\varepsilon = \int_0^\varepsilon \sigma(\varepsilon)d\varepsilon \qquad (8)$$

Where W_ε is the total energy absorbed per unit volume, and $\sigma(\varepsilon)$ is the pressure at strain ε. The W_ε and strain ε curves are plotted in Figure 8, which shows that the W_ε values of the three porous structures increased with strain ε before the compaction stage. As seen in Figure 8, the W_ε values of the three porous structures become smaller as the porosity increases which was similar to the result mentioned in other study [24]. At the same porosity, the slope of the energy–strain curve per unit volume was larger for the I-WP structure than for the primitive one. This finding indicated that the former had excellent energy-absorption characteristics. The excellent energy-absorbing properties of I-P porous structures are mainly attributed to their unique compressive deformation characteristics. The layer with the lowest mechanical qualities is where the I-P porous structure fails in the compression test, while the remaining portion directly supports the failing layer. This phenomenon suggested that the energy-absorption capacity depended on the stable deformation of the porous structure and only slightly depended on the porosity of the structure.
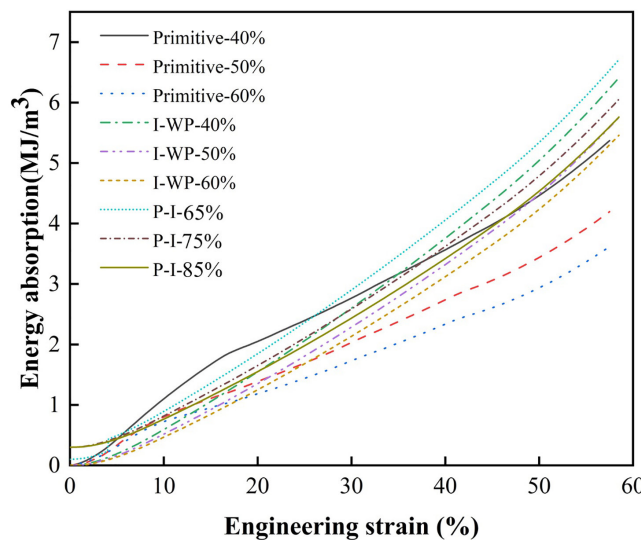

Figure 8: Energy absorption comparison charts of porous structures: (a) primitive; (b) I-WP; (c) P-I.

4. CONCLUSION

Primitive and I-WP porous structures were designed using the implicit function of TPMS. The relationship between porosity $\rho*$ and threshold t was established using MATLAB. The combinatorial optimization of the pinch-off problem arising at a high porosity was conducted to obtain the P-I structure with a high porosity.

The porous structure parameters affected the mechanical and energy-absorption properties of the porous structures. The compressive strength and elastic modulus of the same porous structure type decreased with increased porosity. The compressive strength and elastic modulus of the primitive structures with the same porosity were greater than those of I-WP porous structures. The compressive properties of P-I with a high porosity were better than those of the primitive and I-WP structures. At the same porosity, the I-WP structure showed better energy-absorption properties than those of the primitive structure. The P-I structure with a high porosity had a higher slope of the energy–strain curve per unit volume, indicating better energy-absorption characteristics.

The relationship between the design parameters and mechanical properties of the porous structures was obtained using the Gibson–Ashby formula. The primitive porous structure was predominantly deformed in tensile mode, whereas I-WP and P-I porous structures were predominantly deformed in tensile and bending modes.

5. ACKNOWLEDGMENTS

6. BIBLIOGRAPHY

[1] WANG, Z., WANG, X., GAO, T., *et al*., "Mechanical behavior and deformation mechanism of triply periodic minimal surface sheet under compressive loading", *Mechanics of Advanced Materials and Structures*, v. 28, n. 19, pp. 2057–2069, 2020. doi: http://doi.org/10.1080/15376494.2020.1829756.

[2] YANG, L., YAN, C., HAN, C., *et al*., "Mechanical response of a triply periodic minimal surface cellular structures manufactured by selective laser melting", *International Journal of Mechanical Sciences*, v. 148, pp. 149–157, 2018. doi: http://doi.org/10.1016/j.ijmecsci.2018.08.039.

[3] GAO, B., ZHAO, H., PENG, L., *et al*., "A review of research progress in Selective Laser Melting (SLM)", *Micromachines*, v. 14, n. 1, pp. 57, Dec. 2022. doi: http://doi.org/10.3390/mi14010057. PubMed PMID: 36677118.

[4] LI, Z.-H., NIE, Y.-F., LIU, B., *et al*., "Mechanical properties of AlSi10Mg lattice structures fabricated by selective laser melting", *Materials & Design*, v. 192, pp. 108709, 2020. doi: https://doi.org/10.1016/j.matdes.2020.108709.

[5] LIMA, L.F., MARQUES, V.A.S., SHIMANO, M.M., *et al.*, "Influência da temperatura ambiente no comportamento mecânico do PLA utilizado em manufatura aditiva", *Matéria (Rio de Janeiro)*, v. 27, n. 4, pp. e20220177, 2022. doi: http://dx.doi.org/10.1590/1517-7076-rmat-2022-0177.

[6] BANJANIN, B., VLADIĆ, G., PÁL, M., *et al.*, "Consistency analysis of mechanical properties of elements produced by FDM additive manufacturing technology", *Matéria (Rio de Janeiro)*, v. 23, n. 4, pp. e12250, 2018. doi: http://dx.doi.org/10.1590/S1517-707620180004.0584.

[7] SHEN, M., QIN, W., XING, B., *et al*., "Mechanical properties of 3D printed ceramic cellular materials with triply periodic minimal surface architectures", *Journal of the European Ceramic Society*, v. 41, n. 2, pp. 1481–1489, 2021. doi: http://doi.org/10.1016/j.jeurceramsoc.2020.09.062.

[8] SANTOS, J., PIRES, T., GOUVEIA, B.P., *et al*., "On the permeability of TPMS scaffolds", *Journal of the Mechanical Behavior of Biomedical Materials*, v. 110, pp. 103932, 2020. doi: http://doi.org/10.1016/j.jmbbm.2020.103932. PubMed PMID: 32957226.

[9] PUGLIESE, R., GRAZIOSI, S., "Biomimetic scaffolds using triply periodic minimal surface-based porous structures for biomedical applications", *SLAS Technology*, v. 28, n. 3, pp. 165–182, Jun. 2023. doi: http://doi.org/10.1016/j.slast.2023.04.004. PubMed PMID: 37127136.

[10] PENG, C., FOX, K., QIAN, M., *et al*., "3D printed sandwich beams with bioinspired cores: Mechanical performance and modelling", *Thin-walled Structures*, v. 161, pp. 107471, 2021. doi: http://doi.org/10.1016/j.tws.2021.107471.

[11] RAJAGOPALAN, S., ROBB, R.A., "Schwarz meets Schwann: design and fabrication of biomorphic and durataxic tissue engineering scaffolds", *Medical Image Analysis*, v. 10, n. 5, pp. 693–712, Oct. 2006. doi: http://doi.org/10.1016/j.media.2006.06.001. PubMed PMID: 16890007.

[12] YANG, L., YAN, C., FAN, H., *et al*., "Investigation on the orientation dependence of elastic response in Gyroid cellular structures", *Journal of the Mechanical Behavior of Biomedical Materials*, v. 90, pp. 73–85, 2019. doi: http://doi.org/10.1016/j.jmbbm.2018.09.042. PubMed PMID: 30359855.

[13] LIU, F., MAO, Z., ZHANG, P., *et al*., "Functionally graded porous scaffolds in multiple patterns: New design method, physical and mechanical properties", *Materials & Design*, v. 160, pp. 849–860, 2018. doi: http://doi.org/10.1016/j.matdes.2018.09.053.

[14] LI, D., LIAO, W., DAI, N., *et al*., "Optimal design and modeling of gyroid-based functionally graded cellular structures for additive manufacturing", *Computer Aided Design*, v. 104, pp. 87–99, 2018. doi: http://doi.org/10.1016/j.cad.2018.06.003.

[15] AL-KETAN, O., LEE, D.-W., ABU AL-RUB, R.K., "Mechanical properties of additively-manufactured sheet-based gyroidal stochastic cellular materials", *Additive Manufacturing*, v. 48, pp. 102418, 2021. doi: http://doi.org/10.1016/j.addma.2021.102418.

[16] CECEN, B., "FDM-based 3D printing of PLA/PHA composite polymers", *Chemicke Zvesti*, v. 77, n. 8, pp. 4379–4386, 2023. doi: http://doi.org/10.1007/s11696-023-02786-4.

[17] YOO, D.-J., "Computer-aided porous scaffold design for tissue engineering using triply periodic minimal surfaces", *International Journal of Precision Engineering and Manufacturing*, v. 12, n. 1, pp. 61–71, 2011. doi: http://doi.org/10.1007/s12541-011-0008-9.

[18] ZHANG, C., JIANG, Z., ZHAO, L., *et al*., "Mechanical characteristics and deformation mechanism of functionally graded triply periodic minimal surface structures fabricated using stereolithography", *International Journal of Mechanical Sciences*, v. 208, pp. 106679, 2021. doi: http://doi.org/10.1016/j.ijmecsci.2021.106679.

[19] ABOU-ALI, A.M., LEE, D.W., ABU AL-RUB, R.K., "On the effect of lattice topology on mechanical properties of sls additively manufactured sheet-, ligament-, and strut-based polymeric metamaterials", *Polymers*, v. 14, n. 21, pp. 4583, Oct. 2022. doi: http://doi.org/10.3390/polym14214583. PubMed PMID: 36365578.

[20] AL-SAEDI, D.S.J., MASOOD, S.H., FAIZAN-UR-RAB, M., *et al*., "Mechanical properties and energy absorption capability of functionally graded F2BCC lattice fabricated by SLM", *Materials & Design*, v. 144, pp. 32–44, 2018. doi: http://doi.org/10.1016/j.matdes.2018.01.059.

[21] AL-KETAN, O., ABU AL-RUB, R.K., "Multifunctional mechanical metamaterials based on triply periodic minimal surface lattices", *Advanced Engineering Materials*, v. 21, n. 10, pp. 1900524, 2019. doi: http://dx.doi.org/10.1002/adem.201900524.

[22] MA, Z., ZHANG, D.Z., LIU, F., *et al*., "Lattice structures of Cu-Cr-Zr copper alloy by selective laser melting: Microstructures, mechanical properties and energy absorption", *Materials & Design*, v. 187, pp. 108406, 2020. doi: http://doi.org/10.1016/j.matdes.2019.108406.

[23] FAN, X., TANG, Q., FENG, Q., *et al*., "Design, mechanical properties and energy absorption capability of graded-thickness triply periodic minimal surface structures fabricated by selective laser melting", *International Journal of Mechanical Sciences*, v. 204, pp. 106586, 2021. doi: http://doi.org/10.1016/j.ijmecsci.2021.106586.

[24] ZHAO, M., ZHANG, D.Z., LIU, F., *et al*., "Mechanical and energy absorption characteristics of additively manufactured functionally graded sheet lattice structures with minimal surfaces", *International Journal of Mechanical Sciences*, v. 167, pp. 105262, 2020. doi: http://doi.org/10.1016/j.ijmecsci.2019.105262.